Progress In Electromagnetics Research B, Vol. 13, 357–383, 2009

A PROJECTIVE APPROACH TO ELECTROMAGNETIC PROPAGATION IN COMPLEX ENVIRONMENTS

E. Di Giampaolo and F. Bardati

Dipartimento di Informatica, Sistemi e Produzione
Universita' di Roma Tor Vergata
via del Politecnico 1, Roma 00133, Italy

Abstract—High frequency methods resort to numerical ray tracing for application to complex environments. A new method based on the geometrical projection performed by a ray-congruence has been developed as a preconditioning of the ray tracing procedure. It builds a visibility tree, i.e., a database, storing information on all possible ray paths inside a scenario. The method gives a solution to a class of open problems of ray tracing techniques: ray missing, double (multiple) counting, termination criterion, calculation upgrade. Other features of the method are the multipath map and the multipath classification that allow the user to know the relevance of multipath at any point of the scenario in advance, before ray-tracing calculation.

The method can be systematically applied to scenarios pertaining to different applications provided that the objects belong to the class of polyhedrons. Reflected and diffracted contributions in a scene are modelled as secondary sources which are handled with an off-line electromagnetic field calculation.

Numerical analysis is provided showing the efficiency of the method.

1. INTRODUCTION

Deterministic models based on Geometrical Optics (GO) and Uniform Theory of Diffraction (UTD) [1] are widely used for high-frequency electromagnetic propagation in large and complex environments such as urban, indoor and terrain scenarios, where multipath prediction is suitable for high bit-rate digital communication. Electromagnetic analysis of automotive, ship, and satellite platforms

Corresponding author: E. Di Giampaolo (digiampaolo@disp.uniroma2.it).

also can take advantage of GO/UTD modeling for on-board antenna characterization, coupling, electromagnetic compatibility as well as radar cross section [2–5]. In general, GO/UTD models are advantageous in comparison with other numerical techniques every time constraints on wavelength and scatterer size are satisfied without restriction to a specific application.

Deterministic models require detailed geometrical and morphological information on the propagation environment. Exploiting GO and/or UTD equations, the electromagnetic field is calculated for given positions of source and observer after the ray paths joining the source to the observation point have been determined. Ray-tracing algorithms are used to single out the possible paths between. Ray propagation is affected by multiple interactions with scatterers, so ray tracers are quite laborious requiring a large amount of computational resources. Moreover, they may lose important field contributions and are troubled by the handling of complex geometries, the managing of large interaction orders, and the modeling of higher-order diffraction.

A feature common to all ray tracers is that an increased complexity of the propagation environment requires increasing efforts to determine the whole set of possible ray paths. Therefore the ray propagation models, which have been proposed in the literature, are generally designed for the particular scenario that is analyzed. A number of papers has been published on this subject and a comprehensive review is presented in [6]. Both 2-D and 3-D [7–16], ray tracers have been proposed in the case of urban propagation, similarly for indoor propagation [17–21]. Moreover, to overcome the lack of diffuse radiation due to the roughness of the surfaces ray tracing techniques have been recently improved resorting to diffuse scattering models [22] and radiosity [23]. To improve the computational efficiency instead, some of the proposed algorithms exploit geometrical symmetries, such as vertical symmetry for urban environments. Image based models [10–12] resort to particular visibility algorithms in order to determine visible objects. Another ray-tracing critical feature is the need of a criterion to stop a computation. Indeed, a truncation error occurs when the propagation is stopped at a prefixed interaction order. Recently, a progressive technique [24] has been proposed to counteract the truncation error. Ray missing can be avoided by beam tracers [25–30] which, however, have other troubles in particular in handling diffraction, which is responsible for communication to shadowed (non-line-of-sight) areas.

Even though many ray-tracing models developed over the last years use sophisticated algorithms to reduce the computational charge showing good agreement with measurements, the need of improving

the accuracy and reducing the computational effort is not yet fulfilled. To the best of our knowledge, ray missing, termination criterion and calculation upgrade are still open problems that have been marginally faced in literature. Ray missing mainly depends on the ability of visibility algorithms to determine the visible portion of objects and, in particular, the boundary of objects that causes diffraction. A termination criterion is a set of rules that stop computation (i.e., ray-bouncing) along with knowledge of the truncation error. For brevity we call upgrading ability the property of an algorithm to minimize the additional computational effort that is required by the inclusion of further objects in the environment. Usually, a new complete ray tracing is performed when the environment complexity is increased by addition of details. Upgrading techniques, instead, exploit already calculated data as start point for improved calculation. The calculation upgrade has been used in [31] to take the moving of an object into account.

We base our method on a Projective Scheme (PS) which is independent of any particular application and gives a solution to the above mentioned problems improving accuracy without additional computational charge. It avoids ray missing resorting to the concept of ray congruence, which denotes a family of rays that fill up a portion of the three dimensional space including sources and scatterers. Moreover, the truncation error can be estimated by means of the power-density spreading, which is a geometrical parameter independent of the environment morphology. The upgrading techniques exploit a visibility database in conjunction with the projective scheme. The use of a visibility database may resemble the methods in [10–12] and [29] which also make use of it. While the methods in [10–12] are aimed at determining the visibility of objects in order to accelerate ray tracing computation, our method determines the portion of three dimensional space that is filled with a ray congruence, i.e., a frustum. Once the frustum is obtained no further ray-intersection test is necessary because the rays through a point are found enforcing a belonging test. Our method also overcomes the ambiguity errors typical of beam tracers [29], i.e., a ray contribution shared by adjacent beams may be omitted or counted twice. Including all possible ray-paths, the projective scheme permits to determine any multipath contributions at any point of the scene without making ray-tracing calculation. It allows the user to single out regions of the scene affected by a specific multipath and to restrict the extensive ray-tracing procedure to them.

A projection is a continuous mapping that transforms points in a coordinate system of dimension m into points in a coordinate system of dimension less than m [32]. Let a bundle of rays start from a

surface and impinge on some scatterers. Any ray of the bundle is a projection line and the ray congruence that a ray belongs to defines the kind of projection (e.g., stigmatic, astigmatic). According to the above definition, the reverse rays project the objects (3D) on which the rays impinge onto the surface (2D) from where they start. If a bundle starts from a caustic (e.g., a point or a line), the surface of the corresponding wave-front is used for projection. As a result of the projection, the portions of the scatterers impinged by the ray bundle are mapped onto a subset of the start surface. Due to the property of the projective operator to be continuous, the mapping preserves the environment topology [33]. Topological relationships such as adjacency and belonging are useful to counteract the ambiguity error and to reduce the size of the visibility database.

An n-order ray congruence (n denote the interaction order) is generated by diffraction or reflection or transmission at a geometric element (e.g., a line or a surface) belonging to an object in the scenario that has been lighted by an impinging radiation of order $n-1$. An edge-diffracted ray congruence is modeled by Keller's law, while a reflected or transmitted ray congruence is modeled by Snell's law. The projective scheme makes pairs of visible points passing from the $(n-1)$th to the nth interaction. A ray path is determined by a chain of visible pairs when the interaction order is ranged to an order N.

Arrangement of visibility chains is a complicated matter in the case of complex environment, therefore we have developed an iterative procedure which borrows methods and data structures from Computer Graphics [34]. It collects and stores the visibility information between geometrical elements in a visibility database preserving the hierarchy induced by the interaction order n. The visibility database has the structure of a tree, whose root is the primary source. The data related to the geometrical elements that are visible by the source are stored in first-order ($n = 1$) nodes, while the data pertaining to the elements that are visible through the rays from first-order nodes are stored in second-order nodes, and so on according to the projective scheme. The procedure is completed when an a-priori number of interactions has been reached or the power-density spreading is lower than a given threshold. The algorithm falls in the class of iterative methods since it attempts to model electromagnetic propagation in complex environments by finding successive approximations to the field problem.

The visibility data stored in a tree are used by a subsequent procedure to determine the electromagnetic field at any point inside the scenario. A two-step procedure is used. The first step determines the ray path between the primary source and an observation point by

exploring the visibility tree, while the second step performs the field calculation.

We shall consider scenarios whose objects are polyhedrons with flat and convex facets and straight edges. Even if some scenarios may be oversimplified using the objects of this class, polyhedrons are frequently used in a large number of applications. No further restriction to particular symmetry, shape or application has been introduced. Three kinds of interaction can be envisaged with polyhedrons, i.e., reflection and transmission at facets, diffraction at edges and corner diffraction. Unlike the other interactions, corner diffraction is not explicitly treated in this paper as it is modeled like a stigmatic point source that is described in depth. The space among the objects is filled by a dielectrically homogeneous medium, e.g., a vacuum.

A numerical code implementing the projective scheme has been developed. In order to show its advantages and the computational charge three examples of applications are discussed. Two simple scenes with few objects are used to assess the accuracy of the electromagnetic calculation. The third example refers to a typical urban scenario and is used to test both the reliability and the computational charge.

The paper is organized as follows. The next section will introduce the projection scheme. In Section 3, the algorithm organization will be illustrated, while its main features together with solutions to the termination and upgrading problems will be discussed in Section 4. Results of the numerical analysis will be presented in Section 5. The ray-congruence equations together with details in handling the ray missing problem are summarized in the appendix.

2. THE PROJECTIVE SCHEME

We consider an environment of objects and wavefront-radiating sources. Wavefronts and objects are modeled with an arrangement of polygonal facets. A ray-congruence starts from the surface of objects or wavefronts and impinges on the surfaces of other objects. At the nth iteration, ray-congruences of order $(n-1)$ impinge on the surfaces of some objects after leaving their start surface S^i_{n-1}. A 0-order congruence starts from a wavefront of a primary source.

Consider the ith congruence of order $n-1$, M^i_{n-1}, whose rays have origin at S^i_{n-1} and end at s^i_{n-1}. S^i_{n-1} is known from the previous computational step, while s^i_{n-1} has to be determined. The points of s^i_{n-1} can be projected onto points of S^i_{n-1} using the rays of M^i_{n-1} as projection lines. From a computational point of view, s^i_{n-1} is cut out

from the set $\{\Sigma_p\}$ of all the facets by means of the projection of each facet Σ_p onto S^i_{n-1} and determining the visible portion ω_p of Σ_p, i.e., $s^i_{n-1} = \bigcup_p \omega_p$. The elements of $\{\Sigma_p\}$ are ordered according to their distance from S^i_{n-1}. When the $(p+1)$th facet is projected onto S^i_{n-1}, the corresponding ray bundle can be partially or totally obstructed by the facets from 1 to p, that have been already projected. In other words, the projection Ω_{p+1} of Σ_{p+1} is a portion of the starting surface S^i_{n-1} deprived of the areas that are in visibility with closer facets, i.e.,

$$\Omega_{p+1} \subset S^i_{n-1} - C_p, \tag{1}$$

where

$$C_p = \bigcup_{q=1}^{p} \Omega_q \tag{2}$$

if Ω_{p+1} is empty, then M^i_{n-1} cannot make Σ_{p+1} visible by S^i_{n-1}.

$A_p = S^i_{n-1} - C_p$ is the available area for projection onto S^i_{n-1} of the facets that are more distant than Σ_p, while C_p denotes the complementary of A_p, i.e., $A_p \cup C_p = S^i_{n-1}$. If A_p is empty no other facet is visible by means of M^i_{n-1}. Between ω_p and Ω_p there is a one to one correspondence being one the projection of the other by means of a ray bundle m_p, subset of M^i_{n-1}.

It is worth observing that the space s^i_{n-1} that is visible by S^i_{n-1} through M^i_{n-1}, is dynamically obtained when the counter p is increased from 1 to the number of facets.

An example of the projective scheme is given in Fig. 1 for a ray congruence from a rectangle R as the start surface S^i_{n-1}, and three

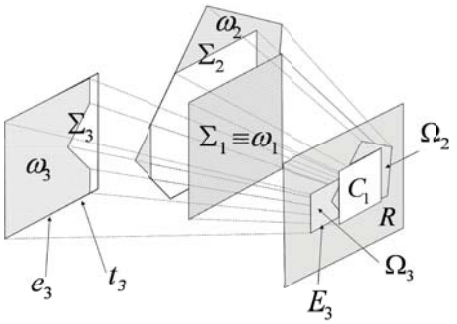

Figure 1. The projective scheme for three surfaces and a ray-congruence from start surface R. Some rays also shown.

facets Σ_p, ($p = 1, 2, 3$) ordered according to their distance from S^i_{n-1}. The ray congruence is stigmatic from a point source not shown in the figure while R is a facet in the wavefront polyhedral approximation. The visible portions (ω_i, $i = 1, 2, 3$) of Σ_1, Σ_2 and Σ_3 are shadowed. Σ_1 is fully visible with footprint Ω_1 coincident with C_1. The visibility of Σ_2 is tested in $A_1 = R - C_1$, and so on.

The boundary Γ_p of Σ_p deserves particular attention when it is projected by M^i_{n-1}. Let t_p denote a side of Γ_p, i.e., a segment of straight line since Γ_p is a polygonal contour. After projection, t_p will be mapped onto a segment T_p of S^i_{n-1}. However, only the portion E_p of T_p that belongs to $S^i_{n-1} - C_p$ is connected by non obstructed rays to a segment $e_p \subseteq t_p$, where C_p is obtained by Equation (2). In this case, e_p is an element of the visible space s^i_{n-1}. If t_p is not a boundary between coplanar facets, then e_p is a diffracting edge. If E_p, e_p are empty sets, no piece of t_p is source of diffracting rays. The construction will be repeated for all the sides of Γ_p and for all p in order to determine the whole set of visible edges $\{e_p\}^i_{n-1}$ that diffract the ray congruence M^i_{n-1}.

In the last step of the nth iteration, s^i_{n-1} is stored as a next-order start surface, S^i_n. S^i_n is the set of the start points of the new ray congruence, M^i_n, obtained by reflection or transmission of M^i_{n-1}. In addition, each element of $\{e_p\}^i_{n-1}$ is source of a diffracted ray congruence. We model a diffracted wavefront from the kth edge as a polyhedral surface, S^k_n [35]. The rays of M^k_n start from the points of S^k_n.

In conclusion to the current iteration, we are left with a set of start surfaces and related ray congruences. Some of them approximate the contours of scatterers and are referred to as material surfaces, while the remaining surfaces that model diffracted wavefronts are purely geometrical. In the next iteration, each one will be propagated to the environment according to the above procedure.

The data related to the geometrical elements s^i_{n-1} is stored in n-order nodes of the visibility tree which are children of an $(n-1)$-order node pertaining to S^i_{n-1}. Data concerns ray-congruence parameters, start surface and impinged surface, while a branch of the tree corresponds to a subset m_p of M^i_{n-1}. As the algorithm makes a partition of the start surfaces into planar polygons for computational convenience, the number of branches from a node can be larger than the number that is strictly necessary to account for reflection, transmission and edge diffraction.

3. ALGORITHM ORGANIZATION

Planar, spherical and cylindrical ray-congruences model primary sources, while astigmatic ray-congruences model wedge diffraction (Appendix B). With the exception of planar ray-congruence, all the others start from caustics, while their wavefronts are curved surfaces that are approximated to polyhedrons in the projective scheme. Wavefronts are approximated preserving the one-to-one correspondence between rays and points of the surface.

The six faces of a cube are used to approximate the spherical wavefront starting from a stigmatic caustic (Fig. 2). Six pyramidal solids W_i, $i = 1, \ldots, 6$ are associated with the faces of the cube. Each W_i has vertex at the caustic point and square cross-section. The ith face is the start-surface S_0^i of the ith ray-congruence M_0^i. The portion of the pyramid W_i lying beyond S_0^i is used by the visibility test.

An astigmatic ray-congruence has a square cylinder as geometrical surface. The cylinder has the axis coincident with the axial caustic. Since an astigmatic raycongruence is bounded in the axial direction by two cones, i.e., the Keller's cones with vertices at the axial-caustic end-points, the cylinder portions beyond the cone/cylinder intersections are cut away. With reference to the cylinder faces, the contour of each face has two straight edges parallel to the axis and two curved edges which are the intersection of the planes for the faces with the cones as shown in Fig. 3. The curved edges are arcs of parabolas that are approximated to polygonal lines. When an astigmatic ray-congruence starts from a wedge by diffraction, the angular sector interior to the wedge is cut out from the cylindrical surface. At the most, four adjacent start-surfaces S_{n-1}^i, $i = 1, \ldots, 4$ are used for projection. The ith volume W_i is a polyhedron having S_{n-1}^i as cross-section and wedges that converge to either of the caustic end-points. The portion of W_i lying beyond S_{n-1}^i is used by the visibility test.

Volume W_i is also said view-volume [32], it is a 3D solid extending to ∞ and filled by a ray-congruence. Its basis is a start surface, e.g., S_{n-1}^i. View-volume shape and size depend on the ray-congruence M_{n-1}^i and the shape of S_{n-1}^i. To speed up computations, we use the view-volume concept to pre-select a subset $\{\Sigma_p\}_{n-1}^i \subseteq \{\Sigma_p\}$ of facets that are candidate to be visible by M_{n-1}^i. For computational purposes, however, the view volume is shortened but its extension remains sufficiently large to include all the facets whose projection falls inside S_{n-1}^i in the absence of obstructions by closer facets. The number of elements in $\{\Sigma_p\}_{n-1}^i$ will be denoted by h. The shortened view-volume is a polyhedron called view-frustum [32].

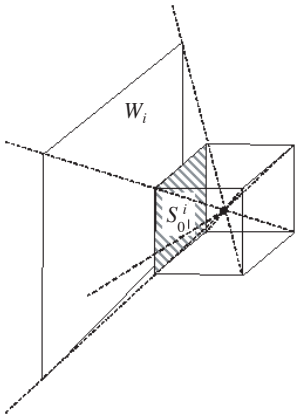

Figure 2. A wavefront from a stigmatic source approximated to a cube. View-volume W_i corresponding to face S^i_0 (dashed) also shown.

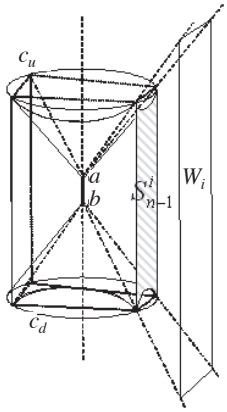

Figure 3. A wavefront from an astigmatic source approximated to four surfaces S^i_{n-1}, $i = 1, \ldots, 4$. View-volume W_i and axial caustic having end-points a, b also shown. c_u and c_d are Keller's cones bounding the view-volume.

To determine the elements of $\{\Sigma_p\}$ inside a view-volume and to sort them according to their distance from the start-surface S^i_{n-1}, a Binary Space Partitioning (BSP) algorithm is used [36]. It is a source independent hierarchical organization of geometrical elements which provides (without additional computational cost) a back-to-front ordering of $\{\Sigma_p\}$ from the surface S^i_{n-1} and reduces the number of candidate surface to be projected for visibility by means of back-face culling and view-frustum culling [32].

At step n, the algorithm projects the elements of $\{\Sigma_p\}^i_{n-1}$ onto S^i_{n-1}. Operatively, each facet Σ_p is projected onto α_q, i.e., onto the plane to which S^i_{n-1} belongs. Due to Σ_p convexity, only the polygonal contour Γ_p is projected. The projection of a point $Q \in \Gamma_p$ is found as the intersection between α_q and the straight-line r_Q passing through Q and belonging to the ray-congruence M^i_{n-1}. The equation for r_Q depends on two parameters that are found by the equations given in Appendix B, in accordance with the type of ray-congruence. Since both plane and spherical ray-congruences project straight lines into straight lines, the shape of Γ_p is preserved after projection, therefore, only the vertices of Γ_p are projected. In general, however, an astigmatic ray congruence projects a straight line, e.g., a side of the contour, into a curve (Fig. B2), because different projecting lines generally belong to distinct Keller's cones. Computationally, such a curved projection is approximated by a polygonal line having vertices at the projections on α_q of suitably sampled points of Γ_p. The set of rays passing through the boundary of the visible portion $\omega_p \subset \Sigma_p$, i.e., $\partial\omega_p$, delimits the portion of the ray-congruence that is impinging on ω_p.

4. ALGORITHM MAIN FEATURES

4.1. Visibility and Ray Missing

The operations on the ith ray-congruence at iteration n of the projective scheme are organized as follows. First the subset $\{\Sigma_p\}^i_{n-1}$ of the h facets that are completely or partially included inside the view-volume is determined, then these facets are sorted according to distance from S^i_{n-1} and projected starting from the nearest surface, and finally secondary sources (i.e., visible surfaces s^i_{n-1} and diffracting edges $\{e_p\}^i_{n-1}$) are determined and stored in the tree database as new branches preserving the parent-child relationship. The iteration arrives to an end when either condition holds: (i) $S^i_{n-1} - C_p = \emptyset$ for some p, i.e., the whole start surface has been mapped onto visible facets/edges; (ii) all the facets of $\{\Sigma_p\}^i_{n-1}$ have been projected. In the last case, $m_\infty = M^i_{n-1} - \bigcup_{p=1}^{h} m_p$ is the ray-bundle that does not impinge any facet while it propagates undisturbed to ∞.

The projective scheme is iteratively applied to all the primary and secondary ray-congruences. At each iteration higher order congruences are generated and stored in new nodes of the tree-database. The computation stops when either a maximum number of reflection/diffraction has been achieved, or power density in ray tubes

is lower than a given threshold as is exposed in Subsection 4.2.

Since the algorithm routinely explores the whole $\{\Sigma_p\}$, no object in the scenario is excluded from the visibility test, therefore it prevents any loss of contribution or twice-counting error from any visible point. This feature is illustrated in Appendix A.

4.2. Termination Criterion

The procedure is stopped when the order n of iteration exceeds a threshold. Alternatively the iteration is stopped when the power density radiated by secondary sources is lower than a threshold. As the algorithm postpones field-strength calculations to a stage that follows projections, we introduce a criterion based on radiated-power spreading factor to determine if that threshold is exceeded.

A source projecting the visible surface $\omega_p \subset \Sigma_p$ onto its image $\Omega_p \subset S^i_{n-1}$, spreads power with a factor

$$sp_p \leq \frac{area\ (\Omega_p)}{area\ (\omega_p)\left(\left|\underline{\hat{n}}_S \cdot \underline{\hat{n}}_p\right|\right)}, \tag{3}$$

where $\underline{\hat{n}}_S$ and $\underline{\hat{n}}_p$ are unit vectors orthogonal to S^i_{n-1} and Σ_p, respectively. Consider now an ordered sequence of N ray-congruences M^i_n, $n = 0, \ldots, N-1$, related to each other by parent-child relationships. The cumulative spreading factor of the sequence is $sp_N = K \prod_{n=1}^{N-1} sp_n$, where K takes into account the primary source which corresponds to $n = 0$, and $K = s^{-2}$ or $K = s^{-1}$ in the case of a stigmatic source or an astigmatic one, respectively. Here s is the minimum distance between the caustic and the start-surface S^i_0. When

$$sp_N < sp_T \tag{4}$$

with sp_T a threshold, M^i_{N-1} contributes to the field at a point P for less than an equivalent source located in the line-of-sight with P at a distance R_P from it. $R_P = {sp_T}^{-1/2}$ if the primary source is astigmatic, while $R_P = sp_T$ if it is stigmatic. Condition (4) is normally used to stop the iterations along each ray bundle from a primary source. It should be noted that, since a planar ray-congruence is still planar after reflection from a flat facet, the cumulative spreading factor is unitary during projective iterations so that the termination criterion has no effect in stopping reflections. A criterion based on the maximum number of iterations is therefore used in such a case.

Some scenarios exhibit different density of scatterers in different regions. In regions with fewer objects the distance between projecting and projected surfaces, ω_p and Ω_p in previous notation, may be so

large that few iterations are normally sufficient to have the spreading factor less than a threshold. On the contrary, a larger number of iterations is often necessary to obtain the desired spreading factor in regions with more objects. For these reasons the stopping criterion based on the spreading factor, if compared to the criterion based on the maximum interaction order, has the advantage of reducing the number of secondary ray-congruences and iterations in some regions of the scenario shortening the computational time and reducing the size of the visibility-tree.

4.3. Calculation Upgrade

To show this feature we consider the simple environment depicted in Fig. 1, where the ray congruence starting from a rectangle, R, projects the visible portions ω_i of Σ_1, Σ_2 and Σ_3 into Ω_i, ($i = 1, 2, 3$). The visibility tree consists of a root node storing the ray congruence through R, three child-nodes storing the reflected ray congruence and several more nodes storing diffracted ray congruences. If a new object, Σ_4, is included in the environment (Fig. 4) the new visibility tree can be obtained without making a new calculation. The previously calculated visibility tree can be augmented by addition of a sub-tree that take into account shadowing, reflection and diffraction by Σ_4. The shadowing by Σ_4 is also a frustum, which intersects the objects placed behind Σ_4 (Fig. 4). The projection of that shadow partially obscures the reflected and diffracted ray congruences from Σ_1 and Σ_2 as well as higher order ray congruences. To take this shadowing into account the existing visibility tree should be modified by subtracting the shadowing frustum from all the obscured ray congruences. As an alternative, the computation of shadowing can be postponed to the procedure for ray-path determination (Subsection 4.4).

The use of upgraded visibility trees is particularly useful for

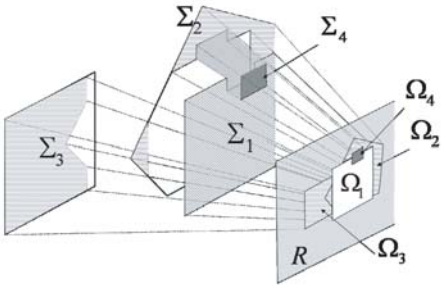

Figure 4. The scene of Fig. 1 is enhanced with facet Σ_4. The shadowing frustum behind Σ_4 also shown.

environments with moving and standing objects. A preliminary calculation determines the static visibility tree neglecting the moving objects, then the sub-tree of a moving object is appended to the static tree in order to perform field calculation and then is removed. As this kind of scenarios are time variant, the time domain analysis is performed by means of a sequence of snapshots of the scene. For each snapshot only the sub-trees of moving objects are calculated. This procedure has been used in [31] for the electromagnetic characterization of inter-vehicle communications.

4.4. Field Analysis

The tree-database calculation is performed only once for a given scenario and source position while the field can be calculated at any point of the 3D space exploiting information stored into the database. Field calculation is under the user control and can be repeated any time changing the observation point as well as parameters concerning the morphology of the scenario and antennas.

Including all possible ray-paths, the visibility tree permits to determine any multipath contributions at any point of the scene without making extensive ray-tracing calculation. For a given sub-domain of the scene (e.g., a plane) the user can visualize all ray-congruences passing through it. If the sub-domain is a plane, a map of the multipath is obtained as superposition of the footprints (i.e., the cross-sections) of the ray-congruences passing through the plane. Consequently, if the user is searching the field due to particular multipath contributions, he can exploit this map to single out the regions of the sub-domain affected by that particular multipath. The ray-tracing procedure can be restricted to these regions neglecting the others. Moreover, a classification of the strength of multipaths can be made on the basis of the cumulative spreading factor. These features permit to speed up the analysis of multipath in large and complex scenes like an airport [39].

To determine the field at a point P inside the scenario a two-step procedure is used. First the ray-paths from a primary source to P are determined by exploiting the data stored in the visibility tree, then the field is calculated along all ray-paths, the total field at P resulting as their vector sum.

The start-surfaces $\{S^i_{m,\,P}\}$ (or ray-bundles $\{M^i_{m,\,P}\}$) which are in line-of-sight with P, are those whose view-frustum includes P. Index m varies from 0 to N according to the order of the interaction. They form a subset of the visibility-tree nodes and are easily found exploring the visibility tree and checking that P belongs to their view-frustum.

This is the only test to determine whether a specific ray is passing through a point. To determine the folded ray path between each node and the primary source, we explore the visibility tree from that node to the root by following a path through the branches, with no jumps. Doing this, an ordered sequence of start-surfaces S_n^i (or ray-bundles M_n^i) is determined starting from $S_{m-1,\,P}^i$. Each ray path is a polygonal line in 3D-space, with vertices at $P_n^i \in S_n^i$, when the interaction level n ranges from 0 to m. From a computational point of view, the vertices are determined starting from P, with sequential projections using Equations (B1)–(B3) and (B5) in accordance with the type of ray-congruence.

Field calculation is performed applying GO/UTD equations to the folded ray path. While the geometrical information useful to electromagnetic field computation (e.g., path length, curvature radius, spreading factor) is gathered during ray-path calculation, data on the primary-source radiation properties, as well as operation frequency and material properties of objects can be arbitrarily inserted by the user. This step can be repeated any time.

5. NUMERICAL ANALYSIS

A numerical code implementing the algorithm has been developed. In order to show the usefulness of the projective approach and its computational charge three examples of application are discussed. Two simple scenarios with few objects are used to assess the accuracy of the electromagnetic calculation. They were previously used in [40] and [41], where both measurements and simulated data are reported. As a third example a typical urban scenario [42] is analyzed to test both the reliability of calculations and the computational charge. Since computational requirements as well as visibility-tree size increase with the scenario's complexity and the number of interactions, an urban scenario represents a good test bed. In each example the primary source is a spherical ray congruence with the radiation pattern of the antenna used in the measurement.

In order to evaluate the effects of many reflected and diffracted contributions, the first scenario consists of a scaled model of urban environment including three perfect-electric-conductor (PEC) objects [40], a transmitter and a receiver. Fig. 5 shows the geometry together with the ray-paths contributing to the field at the receiver point.

The field has been calculated at points belonging to a vertical line partially in line-of-sight with the transmitter. In order to compare our calculation based on a threedimensional model with that published

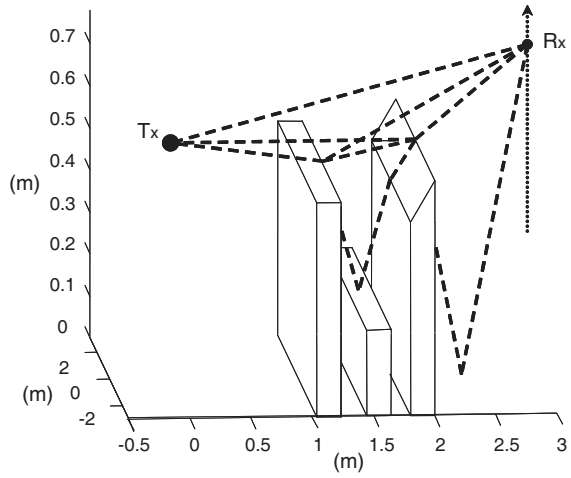

Figure 5. A scaled model of three buildings with PEC walls on a ground. Ray paths to an observation point on a vertical line also shown (dashed lines).

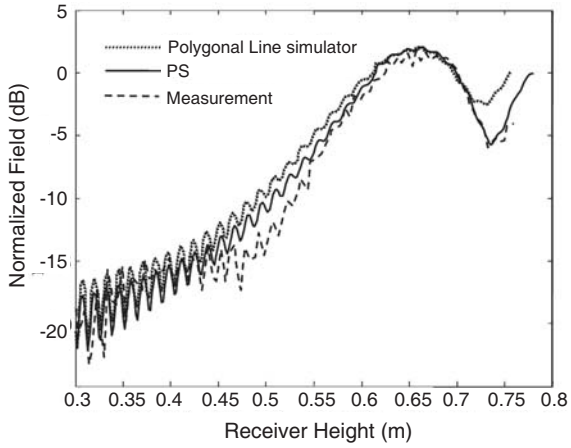

Figure 6. Comparison between PS algorithm and published results for the scene in Fig. 5. Hard-polarization of electric field is shown.

in [40] which is based on a two-dimensional model (Polygonal Line Simulator), only the rays belonging to the plane of symmetry have been considered. A comparison is shown in Fig. 6 pertaining to the hard component of the received field. Grazing incidence has been also taken into account. Numerical results are in excellent agreement with

published data.

The second example consists of two PEC boxes (Fig. 7). It is a full 3D model [41] where both measurements and simulations have been performed without exploiting symmetry. The field is sampled at points of a line placed behind the boxes and partially in line-of-sight with the transmitting antenna. Diagrams in Fig. 8 compare our calculation with measurements and the Fresnel-Kirchhoff method used in [41]. A high degree of correspondence with published measurements and diagrams has been achieved.

Being three-dimensional UTD-based, the proposed method has the advantage to be computationally easier than the Fresnel-Kirchhoff integral method which belongs to the class of integral equation based methods and more effective than the PL method which, being two-

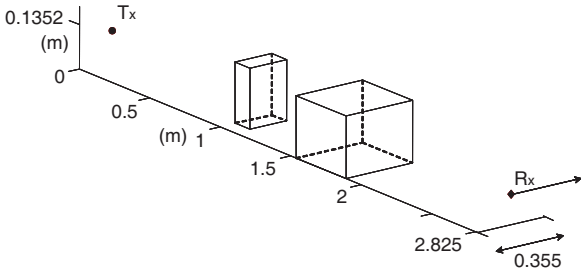

Figure 7. A scene with two PEC boxes.

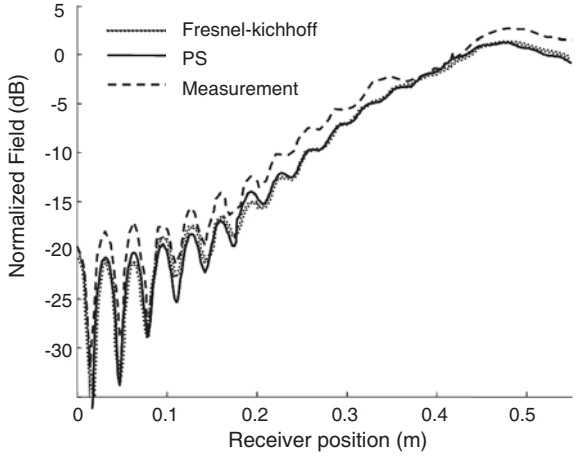

Figure 8. Comparison between our model and published results for the scene of Fig. 7. Horizontal polarization of electric field is shown.

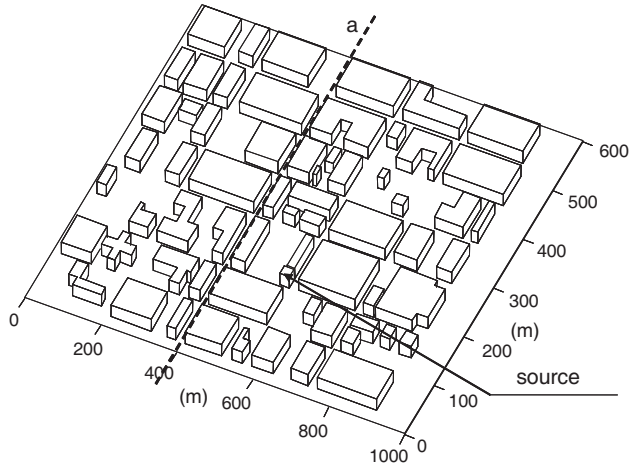

Figure 9. A model of urban environment.

dimensional UTD-based, neglects reflected and diffracted contributions outside the plane where it is working.

The urban scenario shown in Fig. 9 consists of 64 buildings with 432 facets, 910 edges and ground. Ground and buildings are dielectrically homogeneous with relative permittivity $\varepsilon_r = 7$ and conductivity $\sigma = 0.2\,(\mathrm{S/m})$ while the height of each building is higher than the source position. The source is a half-wavelength dipole at 910 MHz located at 8.5 m from ground as shown in Fig. 9, where the dashed line labeled (a) shows the points where the electromagnetic field has been calculated. Field points are at 3.65 m above the ground in the middle of the street. The distance between two consecutive points is 1 m.

Maps of multipath superimposed to the topographic map are shown in Fig. 10. Each map concerns the footprints (grey areas) of ray-congruences passing through a horizontal plane close to the ground. For clarity, different contributions are shown in distinct maps. Fig. 10(a) concerns the ray-congruence starting from the primary source, i.e., it maps the set of points that have a line of sight with the source. Fig. 10(b) shows the map of first-order ray-congruences reflected from vertical walls (for clearness ground reflected ray-congruences are omitted). Fig. 10(c) shows the tenth-order reflected ray-congruences while Fig. 10(d) shows the map of first order diffracted ray-congruences. It is easy to see that the field at the points of the sampling line (a) is mainly affected by diffracted and higher-order reflected contributions. The path loss is shown in

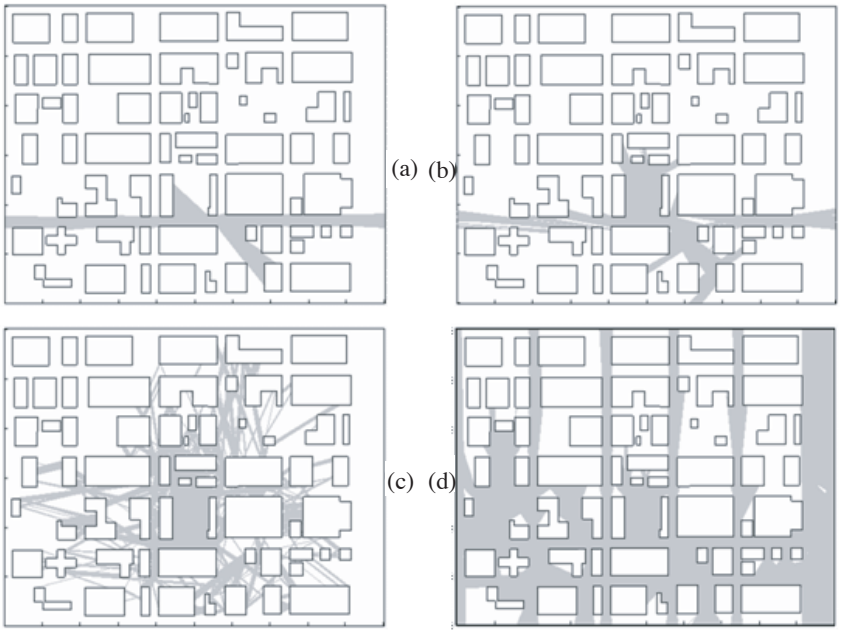

Figure 10. Multipath maps (grey areas) of direct (a), 1st-order reflected (b), 10th-order reflected (c) and 1st-order diffracted, (d) contributions.

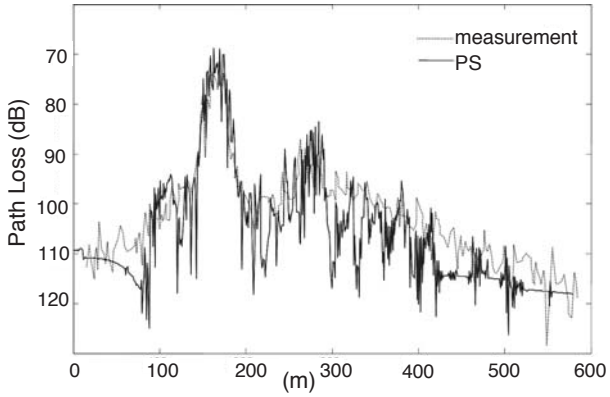

Figure 11. Path loss along sampling line (a) in Fig. 9 and comparison with published results.

Fig. 11 together with published measurements [42]. In spite of the incomplete knowledge of the scenario's characteristics which has been reconstructed starting from the topographic map shown in [42], the agreement with published diagrams is fair. To test the computational charge reflections are calculated up to the tenth order while only first order diffraction is considered. The overall computational time is just over 100 s. The time for storing the visibility tree is about 100 seconds while few seconds are necessary for field calculation at 600 points of line (a). Also few seconds are necessary to visualize a multipath map. The computational time is a fraction of second for the two other scenarios. Computations have been performed with a portable PC Pentium Mobile at 2.0 GHz and 512 MB of RAM).

6. CONCLUSION

The proposed PS tracer exploits geometrical tools for GO/UTD field computation in complex environments with polyhedral objects. Direct transmission, reflection and edge diffraction are included in the tracer. The visibility test between any two elements in the scenario is performed according to a projective scheme that makes the tracer free from missing or ambiguity errors. Ray-paths between a source and observation points are calculated exploring the database. While the visibility database is calculated only once for a given scenario and primary source, field computation can be repeated with less computational cost changing observation points and parameters such as frequency and materials. The results of the numerical analysis show that the tracer is accurate and fast. The projective scheme here has been proposed in the frame of a backward tracer marching from observation points to primary sources. A forward ray-tracer where rays are shot and bounced can also take advantage of the projection method, because the ray density from secondary sources can be arbitrarily fixed by a solver thus avoiding both aliasing and receiving sphere problems that are typical of most existing forward ray-tracers.

Finally, including all possible ray-paths, the visibility tree allows us to know which ray-congruences contribute to the field at an observation point before the field calculation. Moreover, the multipath map permits to visualize the regions of a scene affected by a particular multipath and provides information to sort ray-congruences according to the strength of their contribution. These features can be exploited in progressive prediction models allowing an easy clustering and ordering of rays.

APPENDIX A. RAY MISSING AND AMBIGUITY ERROR

In some beam tracers the decision whether an individual ray belongs to either adjacent beams is a source of error since a contribution may be omitted or counted twice. In this subsection we show that PS algorithm does not have these drawbacks.

Assuming that each Σ_p is a planar convex polygon we denote its footprint by Ω'_p in the absence of obstructions by closer objects. Since the projection operator is continuous, a line segment $u \subset \Sigma_p$ connecting any pair of points of Σ_p, has a unique image $U \subset \Omega'_p$ after projection. The intersection $U \cap A_{p-1}$, if non-empty, belongs to Ω_p and is the projection of the visible portion of u. We assume that whether a point lies in the interior of a given region can be numerically assessed without error. The projective scheme therefore prevents any loss of contribution or twice-counting error from any visible internal point.

It is not yet excluded, however, that these errors can be localized at the boundaries. To discuss this case, let t_p be a side of the contour that is projected onto T_p. Evidently T_p belongs to the boundary of Ω'_p. It is easily verified that, for $p > 1$, t_p is visible if, in addition, T_p is a side of the boundary of $A_p = A_{p-1} - \Omega_p$. Alternatively, the following criterion can be adopted, which is preferable from a computational point-of-view:

$$\text{if } T_p \subset A_{p-1} \text{ then } t_p \text{ is visible} \tag{A1}$$

In Fig. A1, first a partition of S^i_{n-1} into A_{p-1} and C_{p-1} is shown. The two areas are shadowed and clear, respectively. Then Ω'_p is subtracted to produce a new partition of S^i_{n-1} into A_p and C_p. The Ω'_p contour is split into two parts that lie inside A_{p-1} (bold line) and C_p (dashed line), respectively. They are the visible and non-visible parts of the contour, in that order. Enforcing test (A1) on T_p avoids the missing of a possible contribution by t_p. Test (A1) is repeated for all the sides of Σ_p. It is based on the assumption that A_{p-1} is an open set, i.e., it does not contain its boundary. However, to prevent any ambiguity owing to

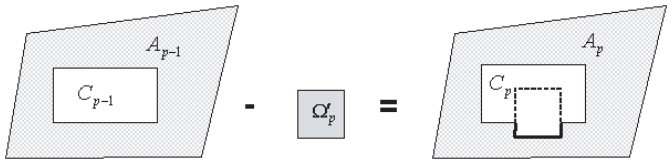

Figure A1. Finding the visible and non-visible portions of a facet, projected as Ω'_P in absence of obstructions, and of its boundary.

Figure A2. A boundary T_p shared by two facets. The facet closer to the ray start-surface already recognized as visible.

numerical computation, if test (A1) is not fulfilled the following further test can be enforced:

$$\text{if } T_p \subset C_p \text{ then } t_p \text{ is non-visible} \tag{A2}$$

To discuss the missing and twice-counting errors, we observe that a side t_p can be shared by two adjacent facets, Σ_p and Σ_q, belonging to the same material surface, so that T_p and T_q coincide on a linear segment U. In another case, Σ_p and Σ_q are not adjacent since they belong to different material surfaces, but the projections T_p and T_q coincide on U. Assume $p > q$, i.e., Σ_q is closer to S^i_{n-1} than Σ_p, so that t_q has already been recognized as visible. A properly designed procedure has to recognize t_p as non-visible. Two cases are possible, according to whether C_{p-1} and Ω'_p lie on the same side with respect to T_p or not, as shown in Fig. A2(a) and Fig. A2(b), respectively. In both cases test (A1) is not passed because T_p does not lie in the interior of A_{p-1}, while test (A2) is passed, confirming t_p as non-visible.

APPENDIX B. RAY CONGRUENCE EQUATION

In any ray-congruence radiated by a source, each ray is determined by the point the ray has in common with a reference surface S, i.e., a wavefront, where the initial conditions: ray-direction, wave amplitude and eikonal are given.

The ray-congruence equation depends on two parameters specifying such a point. S is a plane for a plane wave congruence. In a local Cartesian frame with the z-axis normal to S, the ray for a point $\underline{Q} \equiv (x, y, z)$ has the general equation

$$\begin{aligned} \underline{r}(t) &= u\underline{\hat{x}} + v\underline{\hat{y}} + t\underline{\hat{z}} \\ u &= \underline{Q} \cdot \underline{\hat{x}} \\ v &= \underline{Q} \cdot \underline{\hat{y}} \end{aligned} \tag{B1}$$

where the projections u, v label the ray and t is the distance of Q from S. $\hat{\underline{x}}$, $\hat{\underline{y}}$, $\hat{\underline{z}}$ are unit vectors parallel to the axes. Underlining is used here to distinguish between a geometrical point, Q, and its representation, $\underline{Q}$, as the vector pointing Q from the origin.

In spherical coordinates t, θ, ϕ, the spherical ray-congruence with origin at a point $\underline{r}_0$ has the equation

$$\underline{r}(t) = t\hat{\underline{s}}(\theta, \phi)$$

with $\hat{\underline{s}}(\theta, \phi) = \hat{\underline{x}} \sin\theta\cos\phi + \hat{\underline{y}} \sin\theta \sin\phi + \hat{\underline{z}} \cos\theta$ and t the distance of $\underline{r}$ from $\underline{r}_0$. The ray for a point $\underline{Q}$ is labeled by θ, ϕ that are given by

$$\theta = \arccos\left(-\frac{\underline{Q}\cdot\hat{\underline{z}}}{|\underline{Q}|}\right) \tag{B2}$$

$$\phi = \begin{cases} \gamma & (\hat{z}\times\hat{x})\cdot\underline{Q} \geq 0 \\ 2\pi - \gamma \quad \text{if} & (\hat{z}\times\hat{x})\cdot\underline{Q} < 0 \\ 0 & \gamma = 0 \quad \text{or} \quad 2\pi \end{cases} \tag{B3}$$

where

$$\gamma = \arccos\left(\frac{\underline{Q}\cdot\hat{\underline{x}}}{|\underline{Q} - (\underline{Q}\cdot\hat{\underline{z}})\,\hat{\underline{z}}|}\right)$$

Wedge diffraction originates an astigmatic ray congruence starting from the edge. Any wedge-diffracted ray-congruence is described, exactly or approximately, by two linear caustics [35]. The first caustic is a focal line coincident with the edge and is referred to as axial caustic, while the second caustic is an arc of circle with center, O, on the edge and lying on a plane orthogonal to the edge (Fig. B1). Since the Keller's law links the diffraction-cone angle to the diffracting point D, the two parameters labeling an astigmatic ray congruence are an abscissa w along the edge and an angle ϕ around the edge. Considering the edge oriented along the z-axis of a Cartesian reference frame with origin at O, a ray from D is the straight line.

$$\underline{r}(t) = \underline{D} + t\hat{\underline{s}}(w, \phi)$$

with

$$\hat{\underline{s}}(w,\phi) = \frac{R\left(\cos\phi\hat{\underline{x}} + \sin\phi\hat{\underline{y}}\right) + w\hat{\underline{z}}}{\sqrt{R^2 + w^2}} \tag{B4}$$

and t the distance from $\underline{D}$. Here R is the distance between the axial and non-axial caustics.

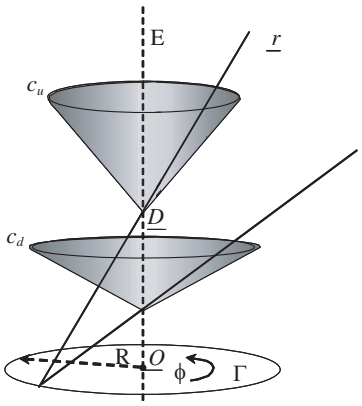

Figure B1. Ray r diffracted at $\underline{D}$. Edge E (vertical line) and circle are caustics. c_u and c_d Keller's cones bounding the astigmatic ray-congruence.

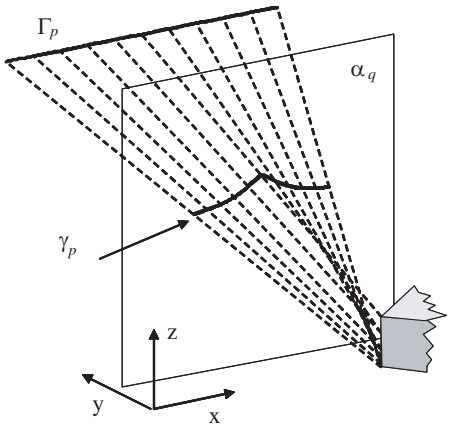

Figure B2. Wedge diffraction: astigmatic projection (curve γ_p) of a straight line Γ_p onto a plane α_q. Projecting rays (dashed line) also shown.

A ray passing through a point Q has parameters

$$w = \frac{R}{R + \left|\underline{Q} - \left(\underline{Q} \cdot \hat{\underline{z}}\right) \hat{\underline{z}}\right|} \left(\underline{Q} \cdot \hat{\underline{z}}\right) \tag{B5}$$

while ϕ is given by (B3).

While $0 \leq \phi \leq 2\pi - \alpha$ where α is the interior angle of the wedge, the domain of w is the axial caustic. The ray-congruence is bounded

by the Keller's cones at the edge end-points.

For $R \to \infty$ we obtain a cylindrical wave with $w = (\underline{Q} \cdot \underline{\hat{z}})$.

REFERENCES

1. Kouyoumjian, R. F. and P. H. Pathak, "A uniform theory of diffraction for an edge in a perfectly conducting surface," *Proc. IEEE*, Vol. 62, 1448–1461, November 1974.
2. Hussar, P., V. Oliker, H. L. Riggins, E. M. Smith-Rowland, W. M. Klocko, and L. Prussner, "AAPG2000: An implementation of the UTD on facetized CAD platform models," *Ant. Prop. Mag.*, Vol. 42, No. 2, 100–106, 2000.
3. Wang, N., Y. Zhang, and C.-H. Liang, "Creeping ray-tracing algorithm of UTD method based on NURBS models with the source on surface," *Journal of Electromagnetic Waves and Applications*, Vol. 20, No. 14, 1981–1990, 2006.
4. Jin, K.-S., T.-I. Suh, S.-H. Suk, B.-C. Kim, and H.-T. Kim, "Fast ray tracing using a space-division algorithm for RCS prediction," *Journal of Electromagnetic Waves and Applications*, Vol. 20, No. 1, 119–126, 2006.
5. Bang, J.-K., B. C. Kim, S.-H. Suk, K.-S. Jin, and H.-T. Kim, "Time consumption reduction of ray tracing for RCS prediction using efficient grid division and space division algorithms," *Journal of Electromagnetic Waves and Applications*, Vol. 21, No. 6, 829–840, 2007.
6. Iskander, M. F. and Z. Yun, "Propagation prediction models for wireless communications systems," *IEEE Trans. Microwave Theory and Technique*, Vol. 50, 662–673, March 2002.
7. Yun, Z., Z. Zhang, and M. F. Iskander, "A ray-tracing method based on the triangular grid approach and application to propagation prediction in urban environments," *IEEE Trans. Antennas Propag.*, Vol. 50, 750–758, May 2002.
8. Rizk, K., J. F. Wagen, and F. Gardiol., "Two-dimensional ray-tracing modeling for propagation prediction in microcellular environments," *IEEE Trans. Veh. Technol.*, Vol. 46, 508–517, May 1997.
9. Liang, G. and H. L. Bertoni, "A new approach to 3-D ray-tracing for propagation prediction in cities," *IEEE Trans. Antennas Propag.*, Vol. 46, 853–863, June 1998.
10. Catedra, M. F., J. Perez, F. Saez de Adana, and O. Gutierrez, "Efficient raytracing technique for three-dimensional analyses of propagation in mobile communications: Application to picocell

and microcell scenarios," *IEEE Antennas Propag. Mag.*, Vol. 40, 15–27, April 1998.

11. Torres, R. P., L. Valle, M. Domingo, and S. Loredo, "An efficient ray tracing method for radiopropagation based on the modified BSP algorithm," *IEEE Veh. Technol. Conference*, Vol. 4, 1967–1971, September 1999.
12. Ng, K. H., E. K. Tameh, A. Doufexi, M. Hunukumbure, and A. R. Nix, "Efficient multielement ray tracing with site-specific comparisons using measured MIMO channel data," *IEEE Trans. Veh. Technol.*, Vol. 56, 1019–1032, May 2007.
13. Fügen, T., J. Maurer, T. Kayser, and W. Wiesbeck, "Capability of 3-D ray tracing for defining parameter sets for the specification of future mobile communications systems," *IEEE Trans. Antennas Propag.*, Vol. 54, 3125–3137, November 2006.
14. Chiu, C.-C. and T.-C. Tu, "Path loss reduction in an urban area by genetic algorithms," *Journal of Electromagnetic Waves and Applications*, Vol. 20, No. 3, 319–330, 2006.
15. Liang, C.-H., Z.-L. Liu, and H. Di, "Study on the blockage of electromagnetic rays analytically," *Progress In Electromagnetics Research B*, Vol. 1, 253–268, 2008.
16. Kara, A. and E. Yazgan, "Modelling of shadowing loss due to huge non-polygonal structures in urban radio propagation," *Progress In Electromagnetics Research B*, Vol. 6, 123–134, 2008.
17. Yang, C.-F., B.-C. Wu, and C.-J. Ko, "A ray tracing method for modeling indoor wave propagation and penetration," *IEEE Trans. Antennas Propag.*, Vol. 46, 907–919, June 1998.
18. Suzuki, H. and A. S. Mohan, "Measurement and prediction of high spatial resolution indoor radio channel characteristic map," *IEEE Trans. Veh. Technol.*, Vol. 49, 1321–1333, July 2000.
19. Teh, C. H. and H.-T. Chuah, "A path-corrected wall model for ray-tracing propagation modeling," *Journal of Electromagnetic Waves and Applications*, Vol. 20, No. 2, 207–214, 2006.
20. Chen, C.-H., C. L. Liu, C. C. Chiu, and T. M. Hu, "Ultra-wide band channel calculation by SBR/IMAGE techniques for indoor communication," *Journal of Electromagnetic Waves and Applications*, Vol. 20, No. 1, 41–51, 2006.
21. Liu, Y.-J., Y.-R. Zhang, and W. Cao, "A novel approach to the refraction propagation characteristics of UWB signal waveforms," *Journal of Electromagnetic Waves and Applications*, Vol. 21, No. 14, 1939–1950, 2007.
22. Degli-Esposti, V., F. Fuschini, E. M. Vitucci, and G. Falciasecca,

"Measurement and modelling of scattering from buildings," *IEEE Trans. Antennas Propag.*, Vol. 55, 143–153, January 2007.

23. Kloch, C., G. Liang, J. B. Andersen, G. F. Pedersen, and H. L. Bertoni, "Comparison of measured and predicted time dispersion and direction of arrival for multipath in a small cell environment," *IEEE Trans. Antennas Propag.*, Vol. 49, 1254–1263, September 2001.
24. Chen, Z., H. L. Bertoni, and A. Delis, "Progressive and approximated techniques in ray-tracing-based radio wave propagation prediction models," *IEEE Trans. Antennas Propag.*, Vol. 52, 240–251, January 2004.
25. Son, H. W. and N.-H. Myung, "A deterministic ray tube method for microcellular wave propagation prediction model," *IEEE Trans. Antennas Propag.*, Vol. 47, 1344–1350, August 1999.
26. Rajkumar, A., B. F. Naylor, F. Feisullin, and L. Rogers, "Predicting RF coverage in large environments using ray-beam tracing and partitioning tree represented geometry," *Wireless Networks*, Vol. 2, 143–154, 1996.
27. Teh, C. H. and H. T. Chuah, "An improved image-based propagation model for indoor and outdoor communication channels," *Journal of Electromagnetic Waves and Applications*, Vol. 17, 31–50, January 2003.
28. Sabbadini, M., F. Bardati, and E. Di Giampaolo, "A recursive beam-splitting algorithm for forward ray tracing," *Proc. USNC/URSI National Radio Science Meeting*, 203, July 1999.
29. Di Giampaolo, E., M. Sabbadini, and F. Bardati., "Astigmatic beam tracing for GTD/UTD methods in 3-D complex environments," *Journal of Electromagnetic Waves and Applications*, Vol. 15, 439–460, April 2001.
30. Di Giampaolo, E., F. Bardati, and M. Sabbadini, "Preconditioned astigmatic beam tracing for urban propagation," *IEEE Microwave and Wireless Components Letters*, Vol. 13, 296–298, August 2003.
31. Di Giampaolo, E., "Electromagnetic characterization of inter-vehicle communications," *IEEE Communications Society, Wireless Rural and Emergency Communications Conference (WRECOM)*, Rome, Italy, October 1–2, 2007,
32. Foley, J. D., A. Van Dam, S. K. Feiner, and J. F. Hughes, *Computer Graphics: Principles and Practice*, Addison-Wesley, Reading, MA, 1990.
33. Di Giampaolo, E. and F. Bardati, "GTD ray tracing by topological

mapping," *Proc. IEEE Antennas and Propag. Society Int. Symp.*, Vol. 1B, 673–676, July 2005.

34. O'Rourke, J. E., "Visibility," *Handbook of Discrete and Computational Geometry*, J. E. Goodman and J. O'Rourke (eds.), 467–479, CRC Press, 1997.
35. Di Giampaolo, E. and F. Bardati, "Analytical model of multiple wedge-diffracted ray congruence," *Electromagnetics*, Vol. 23, 509–524, August 2003.
36. Thibault, W. C. and B. F. Naylor, "Set of operations on polyhedra using BSP trees," *Proc. 14th Annu. Conf. Computer Graphics and Interactive Techniques, SIGGRAPH'87*, Vol. 21, 153–162, August 1987.
37. Di Giampaolo, E. and F. Bardati, "A deterministic tool for multipath propagation modelling," *Proc. IEEE Antennas and Propag. Society Int. Symp.*, Vol. 3, 2231–2234, June 2004.
38. Di Giampaolo, E., "Astigmatic beam tracing for multipath prediction in urban environment," *Proc. URSI EMTS*, 606–608, May 2004.
39. Galati, G., M. Leonardi, E. Di Giampaolo, and S. Barbera, "Multipath evaluation for multilateration systems in complex airport scenario," *Proceedings of International Radar Symposium (IRS)*, September 2007.
40. Erricolo, D., G. D'Elia, and P. L. E. Uslenghi, "Measurements on scaled models of urban environments and comparison with ray-tracing propagation simulation," *IEEE Trans. Antennas Propag.*, Vol. 50, 727–735, May 2002.
41. Xu, Y., Q. Tan, D. Erricolo, and P. L. E. Uslenghi, "Fresnel-Kirchhoff integral for 2-D and 3-D path loss in outdoor urban environments," *IEEE Trans. Antennas Propag.*, Vol. 53, 3757–3766, November 2005.
42. Whitteker, J. H., "Measurements of path loss at 910 MHz for proposed microcell urban mobile systems," *IEEE Trans. Veh. Technol.*, Vol. 37, 125–129, August 1988.